HiSST: International Conference on
High-Speed Vehicle Science Technology
26–29 November 2018, Moscow, Russia

Study on 3D Lattice Boltzmann Method for High-Speed Viscous Flows

Ruofan Qiu[1], Yancheng You, Rongqian Chen, Chenxiang Zhu, Jianfeng Zhu

School of Aerospace Engineering, Xiamen University, Xiamen 361005, PR China

Abstract

The lattice Boltzmann method, which is based on microscopic models and mesoscopic kinetic equations for particle distribution functions, has become a prominent tool in CFD. The 3D lattice Boltzmann method in the framework of coupled double-distribution-function approach for high-speed viscous flows, in which specific-heat ratio and Prandtl number can be adjustable, is developed and studied in this paper. Two types of equilibrium distribution functions are involved, which based on spherical function and Hermite basis, respectively. The two models are tested through numerical simulations of some typical compressible flows, and their numerical stability and precision are also analyzed. The results indicate that the two models are capable for high-speed flows, while the one based on Hermite expansions has numerical stability problem when dealing with compressible flows with shock waves. An artificial viscosity is introduced to enhance the latter model for capturing shock waves and the effect of artificial viscosity is estimated.

Keywords: *Lattice Boltzmann method, three-dimensional, supersonic flows, artificial viscosity, viscous flows.*

Nomenclature (Tahoma 11 pt, bold)

f_α - density distribution function
h_α - total energy distribution function
$\mathbf{e}_\alpha$ - discrete particle velocity in α direction,
τ_f - density relaxation time
τ_h - energy relaxation time
Pr- Prandtl number
ρ - density
$\mathbf{u}$ - velocity
p- pressure
D- dimension of the space
δ_{ij} - Kronecker delta function
E- total energy
T- temperature
μ - viscosity
L- length
Ma- Mach number
Cf- skin friction coefficient

1. Introduction

The lattice Boltzmann method(LBM) has become a prominent tool in computational fluid dynamic(CFD)[1]. Unlike the conventional numerical methods, which are based on discretization of macroscopic governing equations, and unlike the molecular dynamics method, which is based on molecular representation with complicated molecule collision rules, the LBM is based on microscopic models and mesoscopic kinetic equations for particle distribution functions. It simulates fluid flows by tracking the evolutions of the distribution functions and then accumulates the distributions to obtain macroscopic averaged properties. As a mesoscopic numerical method based on the kinetic theory, LBM can describe complex flows from an intuitive view of particle distribution. Its advantages include highly efficiency in parallel computing, complex boundary conditions can be easily formulated in terms of elementary mechanics rules, and simple programming. It has been applied to various fluid applications successfully

[1] School of Aerospace Engineering, Xiamen University, Xiamen 361005, PR China*, E-mail: rf_qiu@xmu.edu.cn*

The basic idea of LBM is to solve discrete Boltzmann Bhatnagar-Gross-Krook(BGK) equation, in which the key issue is distribution function. The distribution function is the discrete velocity Boltzmann equation (DVBE) based method. Once the DVBE model is determined, the fluid flows can be simulated through solving the Boltzmann BGK equaiton directly. The number of DVBE and expression of distribution functions are determined according to specific physical problems. Recently, distribution functions based on spherical function and Hermite expansion are two popular types in high-speed flows.

Although LBM has been well developed in compressible flows, there is a very few 3D compressible LB model, especially for compressible Navier-Stokes equations with a flexible specific-heat ratio and Pr number. Kataoka and Tsutahara presented a D3Q15 model for compressible Euler equations[2]. This model is only for subsonic flow. Chen et al. improved Kataoka and Tsutahara's model for high-speed flow[3]. Watari and Tsutahara proposed a D3Q73 model for Euler equations, which can achieve Mach number 1.7[4]. Li et al. developed Qu et al.'s D2Q13 model[5] to D3Q25 model for compressible Euler equations[6]. He et al. proposed a 3D DDF LB model for compressible Navier-Stokes equations[7]. It can be seen that most 3D compressible LB models are for Euler equations. If the treatments of the existing 2D model for Navier-Stokes equations are complicated, their 3D models will become much more complex.

In this paper, two 3D double-distribution-function (DDF) LB models based on spherical function and Hermite basis for high-speed viscous flow are studied. Moreover, an artificial viscosity is introduced into the Boltzmann-BGK equation to enhance the latter model for capturing shock waves. The rest of the paper is organized as follows. In Section 2, the basic method for constructing DDF LB model is described, and two 3D models are given. In Section 3, numerical simulations are carried out for some

2. Numerical method

2.1. Coupled double-distribution-function approach

The DDF model with a distribution function for density and another for energy, was used for compressible LBM by Li et al. The evolution equations for density and total energy are as follows respectively

$$\frac{\partial f_\alpha}{\partial t}+\left(\mathbf{e}_\alpha\cdot\nabla\right)f_\alpha=-\frac{1}{\tau_f}\left(f_\alpha-f_\alpha^{eq}\right) \tag{1}$$

$$\frac{\partial h_\alpha}{\partial t}+\left(\mathbf{e}_\alpha\cdot\nabla\right)h_\alpha=-\frac{1}{\tau_h}\left(h_\alpha-h_\alpha^{eq}\right)+\frac{1}{\tau_{hf}}\left(\mathbf{e}_\alpha\cdot\mathbf{u}\right)\left(f_\alpha-f_\alpha^{eq}\right) \tag{2}$$

Where f_α is the density distribution function and h_α is the total energy distribution function, f_α^{eq} and h_α^{eq} are the corresponding equilibrium distribution functions, $\mathbf{e}_\alpha$ is the discrete particle velocity in α direction, $\mathbf{u}$ is the macroscopic velocity, τ_f and τ_h are density and energy relaxation times, and τ_{hf} is defined as $\tau_{hf}=\tau_h\tau_f\big/\left(\tau_f-\tau_h\right)$.

The Prandtl number of the system can be made arbitrary by adjusting the two relaxation times as $\mathrm{Pr}=\tau_f/\tau_h$. The macroscopic variables ρ and $\mathbf{u}$ computing from density distribution function are defined as follows:

$$\rho=\sum_{\alpha=0}^{N}f_\alpha \tag{3}$$

$$\rho\mathbf{u}=\sum_{\alpha=0}^{N}f_\alpha e_\alpha \tag{4}$$

The equilibrium density distribution function should satisfy the following velocity moment condition to recover the compressible continuity and momentum equations:

$$\sum_\alpha f_\alpha^{eq}=\rho, \tag{5a}$$

$$\sum_\alpha f_\alpha^{eq}e_{\alpha i}=\rho u_i, \tag{5b}$$

$$\sum_{\alpha} f_{\alpha}^{eq} e_{\alpha i} e_{\alpha j} = \rho u_i u_i + p\delta_{ij}, \tag{5c}$$

$$\sum_{\alpha} f_{\alpha}^{eq} e_{\alpha i} e_{\alpha j} e_{\alpha k} = \rho u_i u_i u_k + p\left(u_k \delta_{ij} + u_j \delta_{ik} + u_i \delta_{jk}\right), \tag{5d}$$

$$\sum_{\alpha} f_{\alpha}^{eq} e_{\alpha}^2 = \rho u^2 + Dp, \tag{5e}$$

$$\sum_{\alpha} f_{\alpha}^{eq} e_{\alpha}^2 e_{\alpha i} = \left[\rho u^2 + \left(D+2\right) p\right] u_i, \tag{5f}$$

The equilibrium total energy distribution should satisfy the following velocity moment condition:

$$\sum_{\alpha} h_{\alpha}^{eq} = \rho E, \tag{6a}$$

$$\sum_{\alpha} e_{\alpha i} h_{\alpha}^{eq} = \left(\rho E + p\right) u_i, \tag{6b}$$

$$\sum_{\alpha} e_{\alpha i} e_{\alpha j} h_{\alpha}^{eq} = \left(\rho E + 2p\right) u_i u_i + p\left(E + RT\right)\delta_{ij}, \tag{6c}$$

Where $E = bRT/2 + u^2/2$ is the total energy.

So far, the framework of coupled DDF LB approach for high-speed with flexible specific-heat ratio and Pr number is given. Once the DVBE model, in which the density distribution function f_{α}^{eq} and the total energy distribution function h_{α}^{eq} satisfy eqs (5) and (6) respectively, is determined for 3D case, the coupled DDF LB model is established.

2.2. Discrete velocity Boltzmann equation model

In this subsection, we show two DVBE models for 3D DDF LB model, in which equilibrium distribution functions are obtained from Spherical function and Hermite basis, respectively.

2.2.1. Spherical function-based model

D3Q25 DVBE model is adopted for the equilibrium density distribution function.

$$e_{\alpha} = \begin{cases} (0,0,0), & \alpha = 0, \\ (1,0,0)_{FS}\,\tilde{c}, & \alpha = 1,2,\ldots,6, \\ (1,1,0)_{FS}\,\tilde{c}, & \alpha = 7,8,\ldots,18, \\ (2,0,0)_{FS}\,\tilde{c}, & \alpha = 19,20,\ldots,24, \end{cases} \tag{7}$$

where $\tilde{c} = \sqrt{3RT_c}$ is the characteristic speed of the lattice fluid, in which T_c is the characteristic temperature, and the subscript FS denotes a fully symmetric set of points.

The 3D equilibrium density distribution functions based on spherical function are given by

$$\begin{aligned} f_0^{eq} = \frac{1}{60}\rho(&60 - 75\bar{r}^2 - 75\bar{u}^2 - 75\bar{v}^2 - 75\bar{w}^2 + 21\bar{r}^4 + 15\bar{u}^4 + 15\bar{v}^4 \\ &+ 15\bar{w}^4 + 70\bar{u}^2\bar{r} + 70\bar{v}^2\bar{r} + 70\bar{w}^2\bar{r} + 60\bar{u}^2\bar{v}^2 + 60\bar{u}^2\bar{w}^2 + 60\bar{v}^2\bar{w}^2), \end{aligned} \tag{8a}$$

$$\begin{aligned} f_1^{eq} = -\frac{1}{90}\rho(&15\bar{u}^4 + 15\bar{u}^3 - 60\bar{u} + 45\bar{u}\bar{r}^2 + 45\bar{u}\bar{v}^2 + 45\bar{u}\bar{w}^2 + 45\bar{u}^2\bar{v}^2 \\ &+ 45\bar{u}^2\bar{w}^2 + 60\bar{u}^2\bar{r}^2 + 15\bar{v}^2\bar{r}^2 + 15\bar{w}^2\bar{r}^2 - 60\bar{u}^2 + 9\bar{r}^4 - 20\bar{r}^2), \end{aligned} \tag{8b}$$

$$f_7^{eq} = \frac{1}{60}\rho(15\bar{u}^2\bar{v}^2 + 15\bar{u}^2\bar{v} + 15\bar{u}\bar{v}^2 + 15\bar{u}\bar{v} + 5\bar{u}^2\bar{r}^2 + 5\bar{v}^2\bar{r}^2 + 5\bar{u}\bar{r}^2 + 5\bar{v}\bar{r}^2 + \bar{r}^4), \tag{8c}$$

$$f_{19}^{eq} = \frac{1}{360}\rho(15\bar{u}^4 + 30\bar{u}^3 + 30\bar{u}^2\bar{r}^2 + 30\bar{u}\bar{r}^2 - 15\bar{u}^2 - 30\bar{u} - 5\bar{r}^2 + 3\bar{r}^4), \tag{8d}$$

and others are

$$
\begin{aligned}
&f_2^{eq}(\bar{u},\bar{v},\bar{w})=f_1^{eq}(-\bar{u},\bar{v},\bar{w}),\ f_3^{eq}(\bar{u},\bar{v},\bar{w})=f_1^{eq}(\bar{v},\bar{u},\bar{w}),\ f_4^{eq}(\bar{u},\bar{v},\bar{w})=f_1^{eq}(-\bar{v},\bar{u},\bar{w}),\\
&f_5^{eq}(\bar{u},\bar{v},\bar{w})=f_1^{eq}(\bar{w},\bar{v},\bar{u}),\ f_6^{eq}(\bar{u},\bar{v},\bar{w})=f_1^{eq}(-\bar{w},\bar{v},\bar{u}),\ f_8^{eq}(\bar{u},\bar{v},\bar{w})=f_7^{eq}(-\bar{u},-\bar{v},\bar{w}),\\
&f_9^{eq}(\bar{u},\bar{v},\bar{w})=f_7^{eq}(\bar{u},-\bar{v},\bar{w}),\ f_{10}^{eq}(\bar{u},\bar{v},\bar{w})=f_7^{eq}(-\bar{u},\bar{v},\bar{w}),\ f_{11}^{eq}(\bar{u},\bar{v},\bar{w})=f_7^{eq}(\bar{u},\bar{w},\bar{v}),\\
&f_{12}^{eq}(\bar{u},\bar{v},\bar{w})=f_7^{eq}(-\bar{u},-\bar{w},\bar{v}),\ f_{13}^{eq}(\bar{u},\bar{v},\bar{w})=f_7^{eq}(\bar{u},-\bar{w},\bar{v}),\ f_{14}^{eq}(\bar{u},\bar{v},\bar{w})=f_7^{eq}(-\bar{u},\bar{w},\bar{v}),\\
&f_{15}^{eq}(\bar{u},\bar{v},\bar{w})=f_7^{eq}(\bar{v},\bar{w},\bar{u}),\ f_{16}^{eq}(\bar{u},\bar{v},\bar{w})=f_7^{eq}(-\bar{v},-\bar{w},\bar{u}),\ f_{17}^{eq}(\bar{u},\bar{v},\bar{w})=f_7^{eq}(\bar{v},-\bar{w},\bar{u}),\\
&f_{18}^{eq}(\bar{u},\bar{v},\bar{w})=f_7^{eq}(-\bar{v},\bar{w},\bar{u}),{}_{20}^{eq}(\bar{u},\bar{v},\bar{w})=f_{19}^{eq}(-\bar{u},\bar{v},\bar{w}),\ f_{21}^{eq}(\bar{u},\bar{v},\bar{w})=f_{19}^{eq}(\bar{v},\bar{u},\bar{w}),\\
&f_{22}^{eq}(\bar{u},\bar{v},\bar{w})=f_{19}^{eq}(-\bar{v},\bar{u},\bar{w}),\ f_{23}^{eq}(\bar{u},\bar{v},\bar{w})=f_{19}^{eq}(\bar{w},\bar{v},\bar{u}),\ f_{24}^{eq}(\bar{u},\bar{v},\bar{w})=f_{19}^{eq}(-\bar{w},\bar{v},\bar{u}),
\end{aligned}
\tag{8e}
$$

where $\bar{u}=u_x/\tilde{c}$, $\bar{v}=u_y/\tilde{c}$, $\bar{w}=u_z/\tilde{c}$ and $\bar{r}=\sqrt{T/T_c}$. Besides, the equilibrium total energy distribution function of the model has the relationship with corresponding equilibrium density distribution function as:

$$
h_\alpha^{eq}=[E+(e_\alpha-\mathbf{u})\cdot\mathbf{u}]f_\alpha^{eq}+\varpi_\alpha\frac{p}{\tilde{c}^2}RT, \tag{9}
$$

where $\varpi_0=0$, $\varpi_{1,2,\ldots,6}=-5.0/14$, $\varpi_{7,8,\ldots,18}=-1.0/7$ and $\varpi_{19,20,\ldots,24}=1.0/14$.

2.2.2. *Hermite expansions-based model*

In the Hermite expansion approach, the equilibrium distribution function can be determined by projecting the Maxwellian function onto the tensor Hermite polynomial basis in terms of the particle velocity and up to a certain order. As pointed out by Shan et al., the Hermite expansion approach allows for simulations of high Mach number flows. Li et al. introduced this method into the DDF LB approach and formulated a thermal model on standard lattices with D2Q9 model. Following this idea, we adopted D3Q27 and D3Q39 standard DVBE model for the 3D coupled DDF compressible model.

The discrete velocities of D3Q27 are given by

$$
e_\alpha=\begin{cases}(0,0,0), & \alpha=0,\\ (1,0,0)_{FS}\,\tilde{c}, & \alpha=1,2,\ldots,6,\\ (1,1,0)_{FS}\,\tilde{c}, & \alpha=7,8,\ldots,18,\\ (1,1,1)_{FS}\,\tilde{c}, & \alpha=19,20,\ldots,26,\end{cases} \tag{10}
$$

where $\tilde{c}=\sqrt{3RT_c}$. And the discrete velocities of D3Q39 are given by

$$
e_\alpha=\begin{cases}(0,0,0), & \alpha=0,\\ (1,0,0)_{FS}\,\tilde{c}, & \alpha=1,2,\ldots,6,\\ (1,1,1)_{FS}\,\tilde{c}, & \alpha=7,8,\ldots,14,\\ (2,0,0)_{FS}\,\tilde{c}, & \alpha=15,16,\ldots,20,\\ (2,2,0)_{FS}\,\tilde{c}, & \alpha=21,22,\ldots,32,\\ (3,0,0)_{FS}\,\tilde{c}, & \alpha=33,34,\ldots,38,\end{cases} \tag{11}
$$

where $\tilde{c}=\sqrt{3RT_c/2}$.

In order to satisfy Eqs. (5) and (6), third-order and second-order Hermite expansion are used for f_α^{eq} and h_α^{eq} , respectively[10]. Therefore, they can be written as follows:

$$
\begin{aligned}
f_\alpha^{eq}=\varpi_\alpha\rho\Big\{&1+\hat{e}_\alpha\cdot\hat{\mathbf{u}}+\frac{1}{2}\Big[(\hat{e}_\alpha\cdot\hat{\mathbf{u}})^2-\hat{u}^2+(\theta-1)(\hat{e}_\alpha^2-D)\Big]\\
&+\frac{\hat{e}_\alpha\cdot\hat{\mathbf{u}}}{6}\Big[(\hat{e}_\alpha\cdot\hat{\mathbf{u}})^2-3\hat{u}^2+3(\theta-1)(\hat{e}_\alpha^2-D-2)\Big]\Big\},
\end{aligned} \tag{12a}
$$

$$
h_\alpha^{eq}=Ef_\alpha^{eq}+\varpi_\alpha p\left[\hat{e}_\alpha\cdot\hat{\mathbf{u}}+(\hat{e}_\alpha\cdot\hat{\mathbf{u}})^2-\hat{u}^2+\frac{\theta}{2}(\hat{e}_\alpha^2-D)\right], \tag{12b}
$$

where $\hat{e}_\alpha = e_\alpha / \sqrt{RT_c}$, $\hat{\mathbf{u}} = \mathbf{u} / \sqrt{RT_c}$, $\theta = T/T_c$ and D is the spatial dimension.

2.2.3. *Artificial viscosity*

We found that many discrete velocity models on Hermite basis are very dispersive and have a strong "oscillating effect" especially near the discontinuities, which results in weak ability of capturing shock waves. For this problem, an artificial viscosity is introduced into present LB model when describing system with shock wave. The artificial viscosity is able to suppress the tendency oscillation and to limit the generation of wiggles and overshoots near shock waves. The artificial viscosity term for Eq. (1) F_v and Eq. (2) H_v are given by[11]:

$$F_v = \theta_{iI} |\kappa_i| \left(1 - |\kappa_i|\right) \frac{\Delta r_i^2}{2\Delta t} \frac{\partial^2 f_\alpha}{\partial r_i^2} \tag{13a}$$

$$H_v = \theta_{iI} |\kappa_i| \left(1 - |\kappa_i|\right) \frac{\Delta r_i^2}{2\Delta t} \frac{\partial^2 h_\alpha}{\partial r_i^2} \tag{13b}$$

where Δr_i is the grid length along i direction, $|\kappa_i|\left(1-|\kappa_i|\right)$ is artificial viscosity coefficient, in which $\kappa_i = u_i \Delta t / \Delta r_i$, and $\theta_{iI} = \lambda \left| \left(p_{iI+1} - 2p_{iI} + p_{iI-1} \right) / \left(p_{iI+1} + 2p_{iI} + p_{iI-1} \right) \right|$ is a switching function that its value is close to 1 in shock while it is close to 0 in other part, in which λ is a parameter that can effect the amplitude. Thus, the artificial viscosity is effective near the shock waves only. F_v and H_v are directly added to the right side of Eq. (1) and Eq. (2), respectively.

3. Numerical results

In this section, the two 3D coupled DDF model are tested by several numerical cases with compressible flows ranging from 1D to 3D. For convenience, the spherical function based model and the Hermite expansions based model are called model I and model II, respectively. To solve Eqs. (1) and (2) numerically, the first-order implicit-explicit(IMEX) Runge-Kutta scheme[8] is employed for the time discretization and the non-free-parameter dissipation (NND) scheme, which is a total variation diminishing (TVD) scheme, is applied for the space discretization. The reference density ρ_0, the reference temperature T_0, the reference length L_0, and the time spacing Δt are used in the simulations, and the reference velocity and the reference pressure are defined as $u_0 = \sqrt{RT_0}$, $p_0 = \rho_0 R T_0$. Here, $\rho_0 = 1.165 kg/m^3$, $R = 287\, J/(kg\,K)$, $T_0 = 303K$, $\mu = 1.86 \times 10^{-5}\, kg/(ms)$, $\tau_0 = \mu / p_0$. The specific heat ratio is set to be 1.4 with b=5 and the Prandtl number is set to be 0.71.

3.1. Riemann problems

The 1D Riemann problem is a typical case for testing numerical methods in simulation of compressible flows. We conducted the Sod shock-tube with initial condition as follows:

$$\left(\rho/\rho_0, \mathrm{u}_x/u_0, p/p_0\right) = \left(1.0, 0, 1.0\right), \quad 0 < x/L_0 \le \frac{1}{2}$$

$$\left(\rho/\rho_0, \mathrm{u}_x/u_0, p/p_0\right) = \left(0.125, 0, 0.1\right), \quad \frac{1}{2} < x/L_0 < 1$$

In the simulations, $T_c = 4/3 T_0$ is set for model I and $T_c = 2T_0$ is set for model II, and $\Delta t = 30000\tau_0$. Simulation results by model I and model II of the Sod shock tube at $t = 0.1644 t_0$ are given in Fig. 1. Generally speaking, the results by the two models agree well with the analytical solutions. Both the two models have some numerical fluctuations about between $x/L_0 = 0.6$ and $x/L_0 = 0.8$, especially for the temperature distribution. This may be caused by the time discretization that just first-order IMEX Runge-Kutta scheme we used. Besides, a little deviation appears at about $x/L_0 = 0.5$ for model II. The magnified results between $x/L_0 = 0.46$ and $x/L_0 = 0.54$ are shown in Fig. 2. Although the same FD schemes the two models used, results by model II disagrees with analytical solutions at about $x/L_0 = 0.5$, while model I still performs well. That is, model II is not very good at simulating compressible flows with discontinuity.

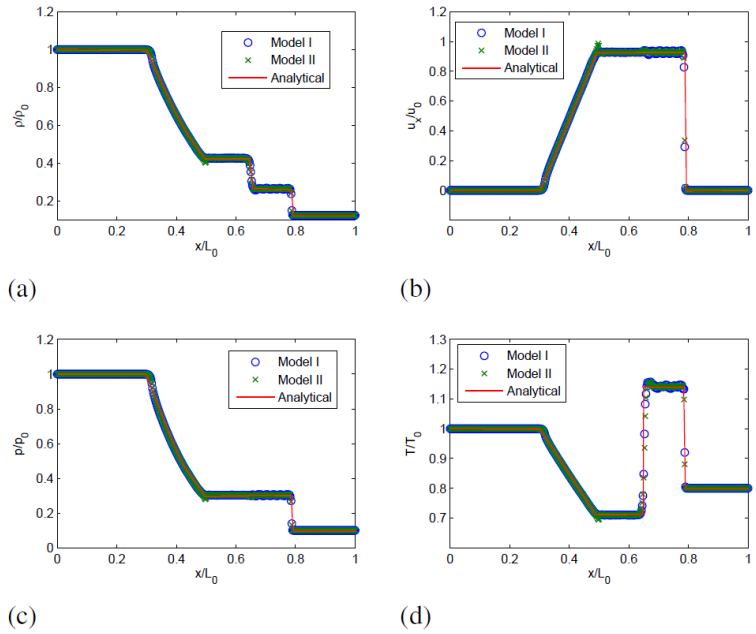

Fig 1. Simulation results by model I and model II of the Sod shock tube for (a) density, (b) velocity, (c) pressure, (d) temperature.

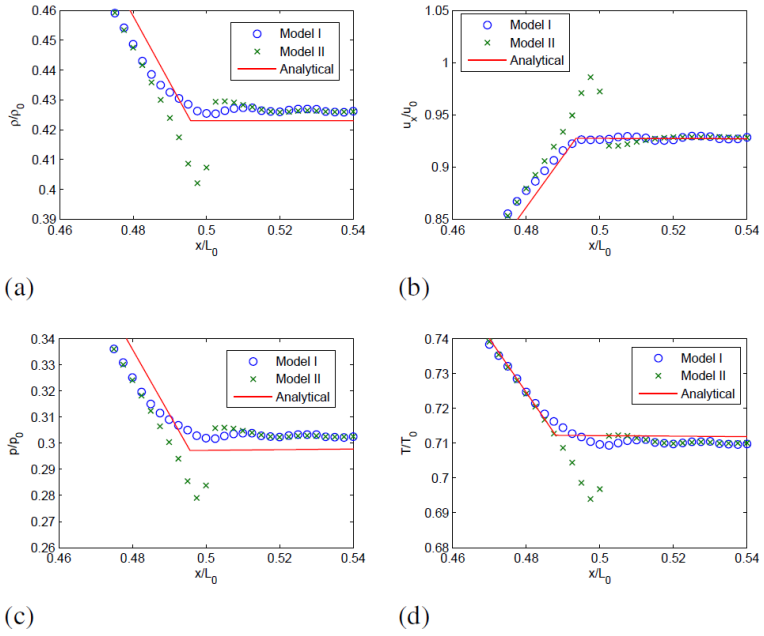

Fig 2. Comparisons of discontinuity between model I and model II in Sod shock tube simulation for (a) density, (b) velocity, (c) pressure, (d) temperature.

To enhance the ability of model II, the artificial viscosity is estimated by tuning coefficient λ. It should be noticed that λ=0 means the artificial viscosity term is not working. The magnified temperature results at the discontinuities are given in Fig. 3, because the deviations in temperature result is larger. As shown in Fig. 3(a), D3Q27 with λ=0 and D3Q27 with λ=15 encounter different degrees of deviations near the discontinuity, while D3Q27 with λ=2 and D3Q39 with λ=0 agree well. The similar conclusion can be drawn from Fig. 3(b). In addition, the D3Q27 with λ=2 performs a little better than D3Q39 with λ=0 at discontinuity near x/L_0=0.8, while the latter is more stable and accurate between the two discontinuities. Through this comparison, D3Q39 model shows better numerical performance than D3Q27 model. Moreover, the appropriate artificial viscosity can enhance ability for capturing discontinuity.

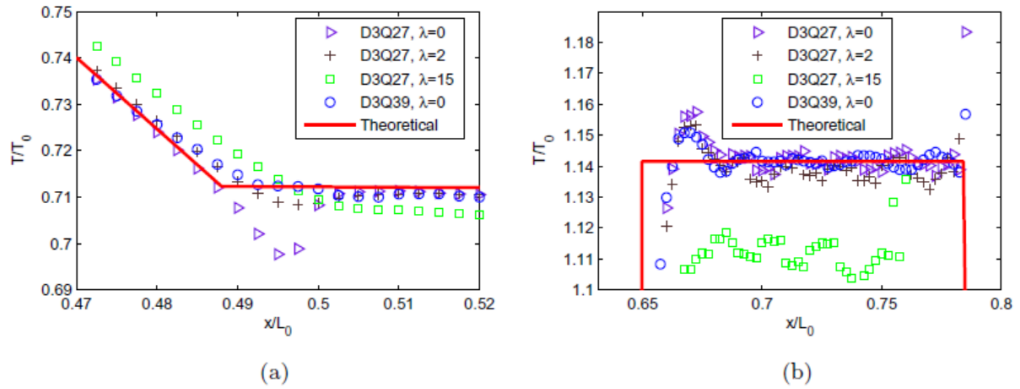

Fig 3. Comparisons of discontinuity of the models in Sod shock tube simulation for temperature result at (a) 0.47<x/L_0<0.52 and (b) 0.63<x/L_0<0.80.

3.2. Regular shock reflection

A steady 2D compressible flow, a regular shock reflection on a wall, is considered in this test. This problem involves three flow regions separated by an oblique shock and its reflection from a wall. The incoming shock wave of Mach number 2.9 has an incident angle to the wall. The Dirichlet conditions

$$\left(\rho/\rho_0, \mathrm{u}_x/u_0, \mathrm{u}_y/u_0, \mathrm{u}_z/u_0, p/p_0\right)|_{Left} = \left(1.0, 2.9, 0, 0, 1.0/1.4\right),$$

$$\left(\rho/\rho_0, \mathrm{u}_x/u_0, \mathrm{u}_y/u_0, \mathrm{u}_z/u_0, p/p_0\right)|_{Top} = \left(1.69997, 2.61934, -0.50633, 0, 1.52819\right).$$

are imposed on the left and top boundaries, respectively. The bottom boundary is a reflecting surface. The right boundary is supersonic outflow where the zeroth-order extrapolation is used. The periodic boundary condition is applied in the z direction. Nx x Ny x Nz = 150 x 50 x 5 lattices are used.

Figure 4 gives numerical results of regular shock reflection problem by model I. In the simulations, Tc=2T0 and $\Delta t = 20000\tau_0$. As shown, the density, velocity, pressure and temperature contours in which the shock reflection is well captured.

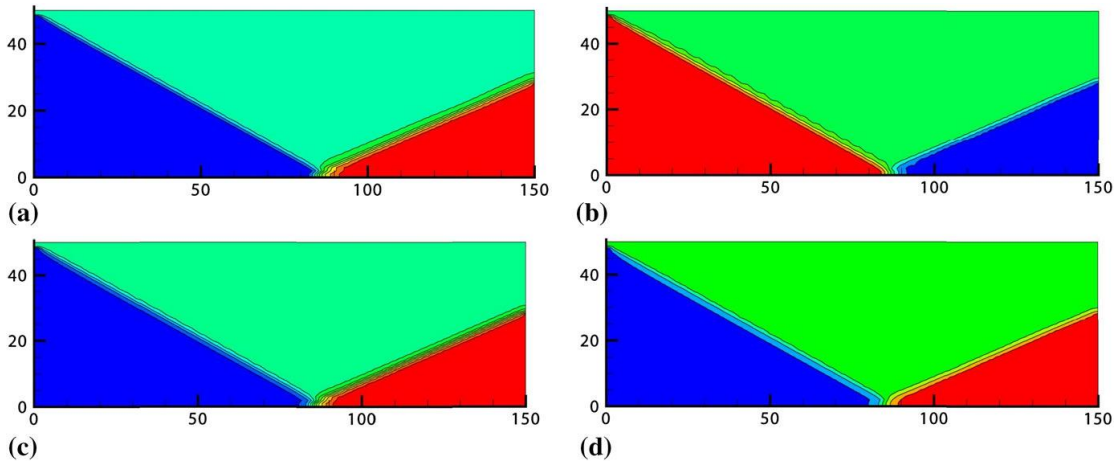

Fig 4. Numerical results of regular shock reflection problem by model I for (a) density, (b) velocity in x direction, (c) pressure, (d) temperature.

Model II with D3Q27 model failed when solving this problem. Then the artificial viscosity is turned on. Figure 5 gives distribution of u_x and T at $500\Delta t$. The fluctuations of flow fields are caused by the poor ability of D3Q27 model for shock wave. The flow fields become more stable as the increasing λ. Nevertheless, even λ is up to 40, the flow fields are still not stable enough. Too large λ will impact numerical precision. Thus, present LBM with D3Q27 model is not suitable for describing shock wave even with the help of artificial viscosity.

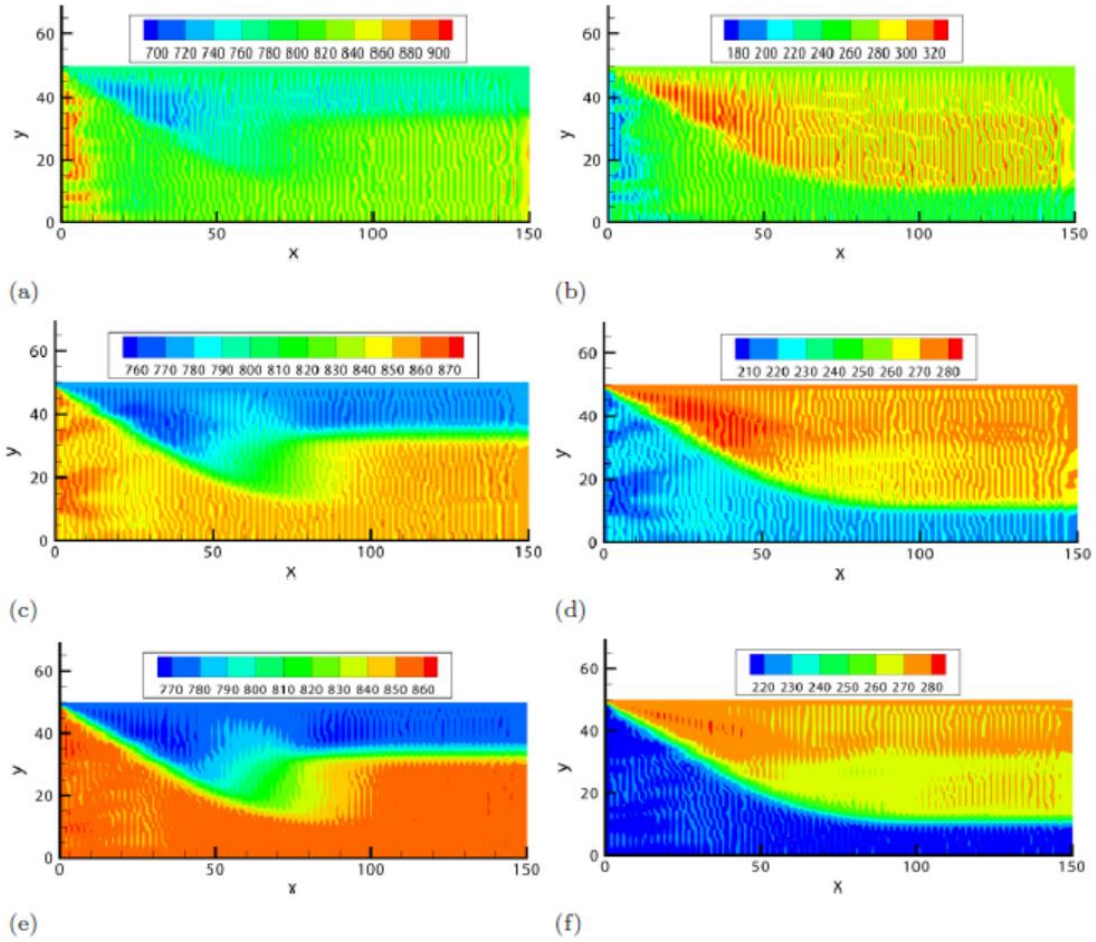

Fig 5. Numerical results of regular shock reflection problem by D3Q27 model at $500\Delta t$ for u_x (left) and T (right), where (a)(b) λ=5, (c)(d) λ=20, and (e)(f) λ=40.

Figure 6 is the results by D3Q39 model II without artificial viscosity. u_x and T at $500\Delta t$ are much stable than the results by D3Q27 model with artificial viscosity shown in Fig. 6. However, large fluctuations appear at $1700\Delta t$. So artificial viscosity is also turned on as given in Fig. 7. u_x and T at $2000\Delta t$ with λ=5 and λ=20 are compared. Both two simulations give clear reflected shock wave result, where shock waves by λ=20 (Fig. 7 (c)(d)) are much stable than the one by λ=5 (Fig. 7 (a)(b)). The incident angle is arctan(48/86)=29.17°, which agrees well with the result 29.05° by Li et al.[9]

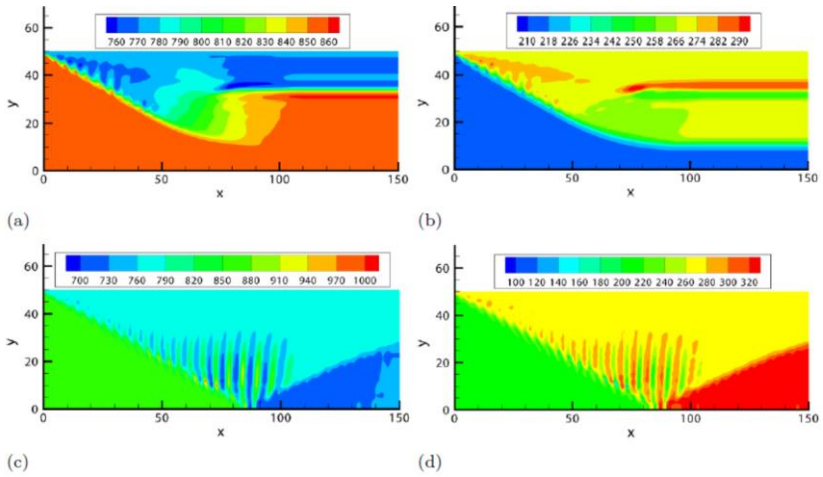

Fig 6. Numerical results of regular shock reflection problem by D3Q39 model with λ=0 for u_x (left) and T (right) at (a)(b) $500\Delta t$, and (c)(d) $1700\Delta t$.

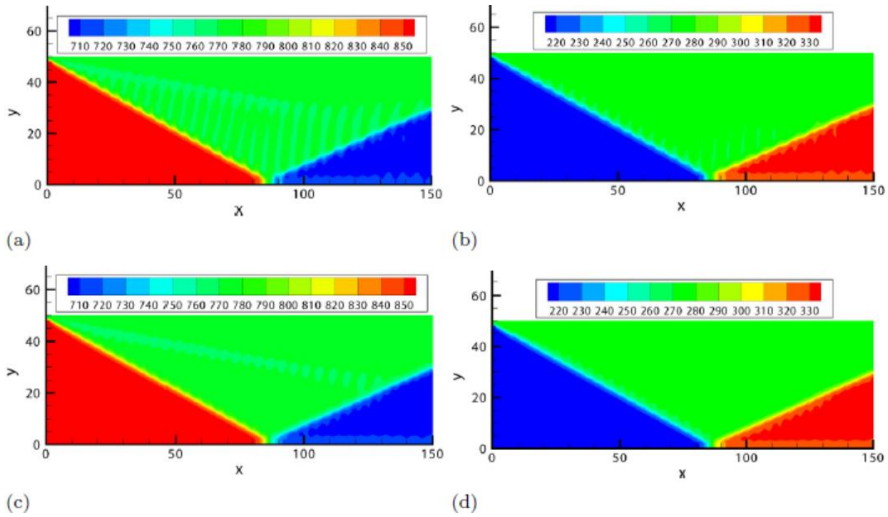

Fig 7. Numerical results of regular shock reflection problem by D3Q39 model for u_x (left) and T (right) at $2000\Delta t$ with (a)(b) λ=5, and (c)(d) λ=20.

3.3. Explosion in a box

The case of 3D explosion in a box[12], in which a spherical shock wave expands in an enclosed box, is tested by the two models. It is an unsteady 3D compressible flow and the reflected shocks interact in a complex manner. The computational domain is [0,1.0] x [0,1.0] x [0,1.0]. At the initial time, the velocity is zero; ρ/ρ_0=5.0 and p/p0=5.0 are set in a sphere with radius 0.3, whose center is at (0.4, 0.4, 0.4), and ρ/ρ_0=1.0 and p/p0=1.0 are set for others.

In the simulations, a Nx x Ny x Nz = 100 x 100 x 100 mesh is used. The rest parameters are set to be T_c=T_0, L_0=1m and Δt=20000τ_0. The model I successfully completes the 3D explosion simulation, while model II becomes unstable after t=0.25t_0. The density isosurfaces at t=0.125t_0, 0.25t_0 and \$0.375t_0 are given in Fig. 8. Figure 9 gives density contour at z=0.4 and t=0.5t_0 by model II of D3Q27 with λ=10, D3Q39 with λ=0 and D3Q39 with λ=10. They are compared with result in Ref.[12], and they all agree well.

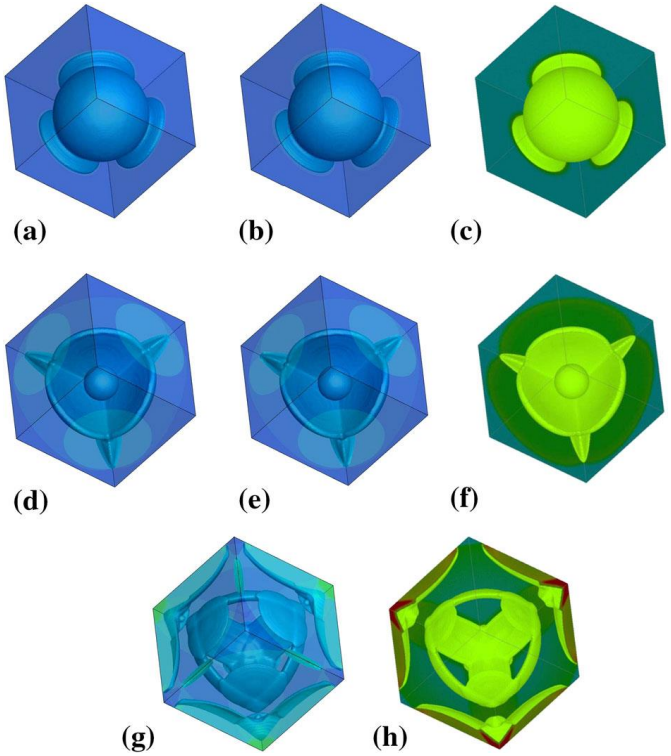

Fig 8. Density isosurfaces of 3D explosion in a box: (a) t=0.125t_0, model I, (b) t=0.125t_0, model II, (c) t=0.125t_0, Ref.[12], (d) t=0.25t_0, model I, (e) t=0.25t_0, model II, (f) t=0.25t_0, Ref.[12], (g) t=0.375t_0, model I, (h) t=0.375t_0, Ref.[12].

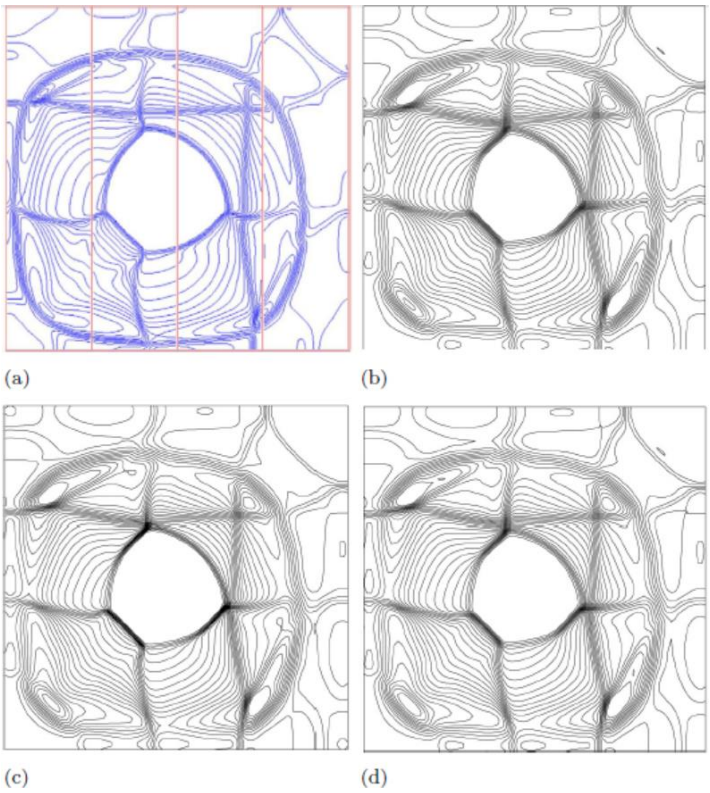

Fig 9. Density contour of 3D explosion in a box at z=0.4 and t=0.5t_0: (a) Ref. [12], (b) D3Q27 with λ=10, (c) D3Q39 with λ=0, and(d) D3Q39 with λ=10.

3.4. Supersonic boundary layer

The compressible boundary layer is a basic and important flow feature in compressible flows. In our previous work, the supersonic boundary layer has been simulated by a 2D LB model[13]. Here, present 3D model is used to simulate the supersonic laminar flow over an insulated flat plate with freestream conditions as Mach number Ma_∞=2, Reynolds number R_∞/L_0=296000/m, Pr=0.72, γ=1.4 and T_∞=293K.

Since there is no shock wave in this case, D3Q39 model without artificial viscosity is adopted with Tc=3.5 and $\Delta t = 3.5\tau_0$. The reference length is set to be L_0=1.0m, which is also the simulation length in x-direction. The length in y-direction Ly and z-direction Lz are 0.1m and 0.2m. The simulations are carried on a Nx x Ny x Nz = 100 x 100 x 40 grid which is equally spaced in the x- and z-direction, and stretched in the y-direction, with an initial y-spacing of $\Delta y = 9.46\times10^{-5}$ m from the plate.. The viscosity is not a constant here, which obeys Sutherland's formula. The boundary conditions are composed of an adiabatic wall boundary along the bottom boundary(y=0), Dirichlet condition with freestream values on the inlet boundary(x=0), supersonic outflow along the outlet(x=Nx) and upper boundaries(y=Ny), period conditions along the two sides(z=0, z=Nz).

Figure 10 shows results of supersonic boundary layer for distributions of p, u_x and T. In the pressure distribution, an expansion wave is formed by the edge of flat plate. For u_x, the velocity near the bottom wall becomes much smaller to develop into supersonic boundary layer. In Fig. 10(c), temperature near the bottom wall is much higher, since the momentum here is transferred into the heat energy. The velocity profiles of boundary layer at different positions are adopted to compare with the theoretical result by Van Driest[14] in Fig. 11. In general, they all agree well. The small deviation appears at u_x/u_∞ >0.8, which also can be observed in our previous work with another 2D LB model. This may be caused by NND scheme, since the result by second order upwind scheme can improve it effectively[13].

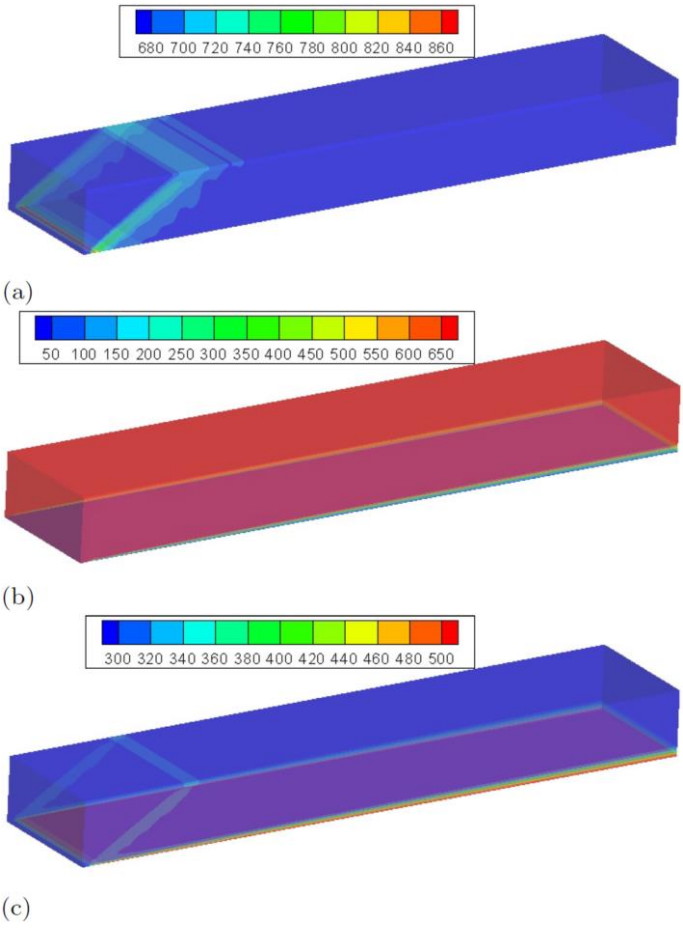

Fig 10. Numerical results of supersonic boundary layer for distributions of (a) p, (b) u_x, and(c) T.

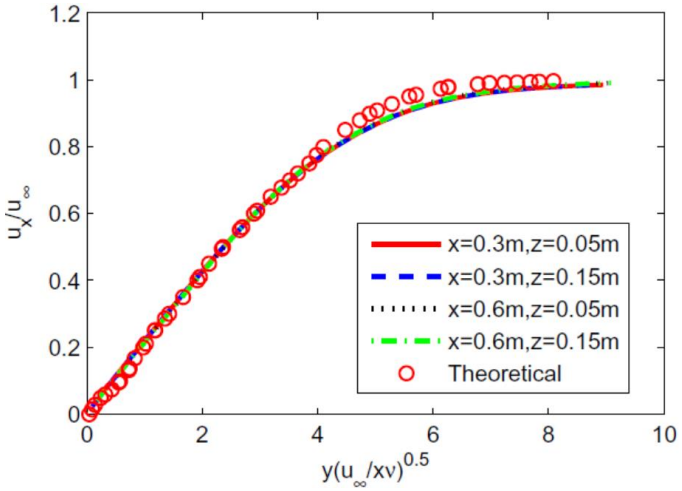

Fig 11. Velocity profiles in a Ma=2 supersonic laminar boundary layer over a flat plate at different positions.

4. Numerical results

In this work, two 3D DDF LB models for compressible flows with flexible specific heat ratio and Pr number are developed. The spherical function based D3Q25 model, and Hermite expansions based D3Q27 model and D3Q39 model are used. Several numerical simulations of some typical compressible flows ranging from 1D to 3D are conducted to test the two 3D models. They are both capable for supersonic flows, while the latter is not very suitable for compressible flows with shock wave. An artificial viscosity is introduced to enhance the model for capturing shock waves. With the help of artificial viscosity, Hermite expansions based LB model with D3Q39 model can handle the discontinuity better. However, D3Q27 model with artificial viscosity is still not suitable for describing shock wave. This work presents alternative LB models for 3D supersonic flows and shows convenience and simplicity of DDF LB approach for complex compressible flows.

References

1. Chen, S., & Doolen, G. D.: Lattice boltzmann method for fluid flows. Ann.rev.fluid Mech, 30(1), 329-364 (1998).
2. Kataoka, T., & Tsutahara, M.: Lattice boltzmann method for the compressible euler equations. Physical Review E Statistical Nonlinear & Soft Matter Physics, 69(2), 056702 (2004).
3. F Chen, A Xu, G Zhang and Y Li.: Three-dimensional lattice boltzmann model for high-speed compressible flows. Communications in Theoretical Physics, 54(12), 1121-1128 (2010).
4. Watari, M., & Tsutahara, M.: Supersonic flow simulations by a three-dimensional multispeed thermal model of the finite difference lattice boltzmann method. Physica A Statistical Mechanics & Its Applications, 364, 129-144 (2006).
5. Qu, K., Shu, C., & Chew, Y. T.: Alternative method to construct equilibrium distribution functions in lattice-boltzmann method simulation of inviscid compressible flows at high mach number. Physical Review E Statistical Nonlinear & Soft Matter Physics, 75, 036706 (2007).
6. Li, Q., He, Y. L., Wang, Y., & Tang, G. H.: Three-dimensional non-free-parameter lattice-boltzmann model and its application to inviscid compressible flows. Physics Letters A, 373(25), 2101-2108 (2009).

7. He, Y. L., Liu, Q., & Li, Q.: Three-dimensional finite-difference lattice boltzmann model and its application to inviscid compressible flows with shock waves. Physica A Statistical Mechanics & Its Applications, 392(20), 4884-4896 (2013).
8. Pieraccini, S., & Puppo, G.: Implicit–explicit schemes for bgk kinetic equations. Journal of Scientific Computing, 32(1), 1-28 (2007).
9. Li, Q., He, Y. L., Wang, Y., & Tang, G. H.: Three-dimensional non-free-parameter lattice-boltzmann model and its application to inviscid compressible flows. Physics Letters A, 373(25), 2101-2108 (2009).
10. Shan, X., Yuan, X., & Chen, H.: Kinetic theory representation of hydrodynamics: a way beyond the navier–stokes equation. Journal of Fluid Mechanics, 550(7), 413-441 (2006).
11. Xu Ai-Guo, Zhang Guang-Cai, Zhang Ping, & Zhang Lei.: Finite-difference lattice boltzmann scheme for high-speed compressible flow:two-dimensional case. Communications in Theoretical Physics, 50(7), 201-210 (2008).
12. Ralf Deiterding: http://amroc.sourceforge.net/examples/euler/3d/html/box3d_c.htm
13. Qiu, R. F., You, Y. C., Zhu, C. X., & Chen, R. Q.: Lattice boltzmann simulation for high-speed compressible viscous flows with boundary layer. Applied Mathematical Modelling, 48 (2017).
14. Van Driest, E. R.: Investigation of laminar boundary layer in compressible fluids using the crocco method. Technical Report Archive & Image Library, 10(1), 15-31 (1952).